



# *In vivo* drug tracking with $^{19}\text{F}$ MRI at therapeutic dose†

 Cite this: *Chem. Commun.*, 2018, 54, 3875

 Received 27th December 2017,  
 Accepted 21st March 2018

DOI: 10.1039/c7cc09898g

rsc.li/chemcomm

 Shaowei Bo,<sup>a</sup> Yaping Yuan,<sup>b</sup> Yongping Chen,<sup>a</sup> Zhigang Yang,<sup>b</sup> Shizhen Chen,<sup>b</sup>  
 Xin Zhou<sup>b</sup> and Zhong-Xing Jiang \*<sup>a</sup>

**Tracking drugs with  $^{19}\text{F}$  MRI would be beneficial for developing theranostics and optimizing drug therapy. To this end, a fluorinated dendritic amphiphile with high  $^{19}\text{F}$  MRI sensitivity and biocompatibility has been developed for  $^{19}\text{F}$  MRI tracking of doxorubicin (DOX)-loaded liposomes in mice, which may provide an effective platform to *in vivo* trace various drugs with  $^{19}\text{F}$  MRI.**

In recent years, many imaging technologies have been developed for *in vivo* drug tracking.<sup>1–7</sup> Among the many imaging modalities, fluorine-19 magnetic resonance imaging ( $^{19}\text{F}$  MRI) is very attractive because it provides quantitative images without ionizing radiation, tissue depth limits, and background signals.<sup>8–11</sup>  $^{19}\text{F}$  MRI has been successfully employed to monitor a variety of cells and biological processes.<sup>12–15</sup> However, it remains a formidable challenge to *in vivo* trace a drug with  $^{19}\text{F}$  MRI. On one hand, the low sensitivity of  $^{19}\text{F}$  MRI, which usually requires a local  $^{19}\text{F}$  concentration over 80 mM to generate high resolution images,<sup>16</sup> excludes the possibility of directly imaging fluorinated drugs *in vivo*.<sup>17,18</sup> Although about 25% of US FDA approved drugs contain at least 1 fluorine,<sup>19,20</sup>  $^{19}\text{F}$  MRI can hardly be generated from fluorine(s) in these drugs due to low *in vivo* drug concentration (usually in the sub-mM range), low fluorine content (usually 1 to 3 fluorine(s) in each drug),  $^{19}\text{F}$  signal splitting, and  $^{19}\text{F}$  signal quenching by interaction with biomacromolecules, *etc.* On the other hand, the synthesis of fluorinated polymer-based drug carriers can increase the local  $^{19}\text{F}$  concentration for  $^{19}\text{F}$  MRI, but it suffers drawbacks such as loss of drug potency, complicated carrier synthesis and drug conjugation,  $^{19}\text{F}$  NMR signal splitting due to the lack of symmetry in the  $^{19}\text{F}$  arrangement, conflicts between fluorine

content and water solubility, undesired organ retention and inherent toxicity of the fluorinated drug carriers, and difficulties in targeted delivery and controlled release.<sup>21–23</sup> It is noteworthy that  $^{19}\text{F}$  MRI tracking of drugs is far more difficult than  $^{19}\text{F}$  MRI tracking of cells because each cell can encapsulate billions of fluorines to improve the local  $^{19}\text{F}$  concentration and no concern for drug conjugation or therapeutic efficacy is necessary.<sup>12,13</sup> Therefore, it would be of great importance to develop novel strategies for *in vivo* drug tracking with  $^{19}\text{F}$  MRI.

To address these challenges, the formulation of a  $^{19}\text{F}$  MRI traceable liposomal drug delivery system may be a good strategy. First, high local  $^{19}\text{F}$  concentration for sensitive  $^{19}\text{F}$  MRI can be obtained by encapsulating a number of either fluorinated drugs or  $^{19}\text{F}$  MRI agents in liposomal nanoparticles.<sup>24–27</sup> Second, non-covalent loading, delivery and release of drugs by liposomes assure high therapeutic indices by avoiding drug potency loss as a result of covalent modification, increasing *in vivo* drug stability, and reducing drug toxicity to normal tissues, *etc.* The tedious case-by-case synthesis, conjugation, and formulation in fluorinated polymeric carrier-based drug delivery systems can be avoided. Third, both fluorinated and nonfluorinated drugs can be monitored by  $^{19}\text{F}$  MRI because the  $^{19}\text{F}$  MRI signal may originate from either fluorinated drugs or  $^{19}\text{F}$  MRI agents incorporated in the liposomes.

Herein, we report a fluorinated amphiphile-based  $^{19}\text{F}$  MRI-traceable liposomal drug delivery system for *in vivo* tracking of DOX with  $^{19}\text{F}$  MRI at its therapeutic dose (Fig. 1). Fluorinated amphiphile **1** was designed as a Janus dendrimer with 3 highly fluorinated moieties as hydrophobic tails and  $^{19}\text{F}$  MRI signal emitters, 3 branched monodisperse polyethylene glycol (M-PEG)<sup>22,28</sup> as hydrophilic heads and solubility, biocompatibility, and stability enhancers. Biocompatible amide bonds were employed to link the moieties. When incorporating amphiphile **1** into liposomes, their stability may be enhanced by strong hydrophobic interactions between multiple hydrophobic tails and the liposomal membrane as well as PEGylating the liposomal surface with multiple branched M-PEG. Basically, both hydrophilic and hydrophobic drugs can be encapsulated in the liposomes. In this proof-of-concept study,

<sup>a</sup> Hubei Province Engineering and Technology Research Center for Fluorinated Pharmaceuticals and School of Pharmaceutical Sciences, Wuhan University, Wuhan 430071, China. E-mail: zxjiang@whu.edu.cn

<sup>b</sup> State Key Laboratory for Magnetic Resonance and Atomic and Molecular Physics, Wuhan Institute of Physics and Mathematics, Chinese Academy of Sciences, Wuhan 430071, China

† Electronic supplementary information (ESI) available: General information, experimental details and additional figures and tables, and synthesis and characterization of compounds. See DOI: 10.1039/c7cc09898g

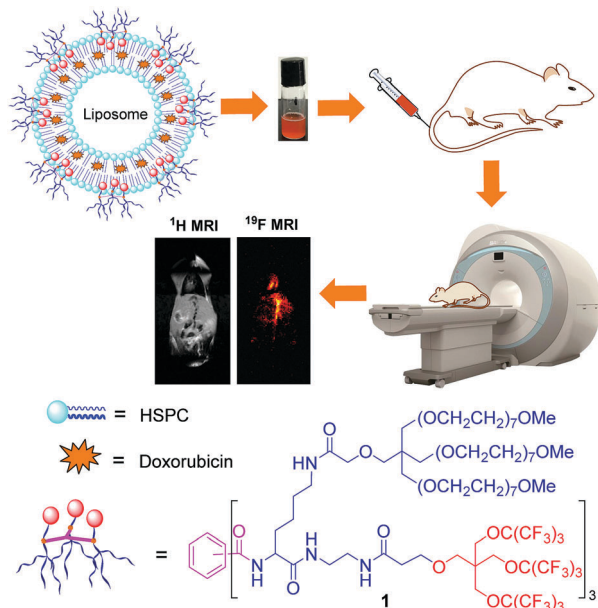


Fig. 1 Design of a  $^{19}\text{F}$  MRI-traceable drug delivery system.

DOX was employed because of its fluorescence properties. Here, high  $^{19}\text{F}$  MRI sensitivity can be achieved in two ways: by improving local  $^{19}\text{F}$  concentration through incorporating multiple amphiphiles **1** into each liposome nanoparticle and by avoiding  $^{19}\text{F}$  NMR signal splitting through a symmetrical distribution of the 81 fluorines in amphiphile **1**.

A convergent synthesis of fluorinated amphiphile **1** (Scheme S1, ESI $^\dagger$ ) was then carried out. From pentaerythritol **2**, triols **3** and **6** were prepared by monoalkylation with allyl bromide and *tert*-butyl acrylate, respectively. After Williamson ether formation between  $\omega$ -methoxy-hepta(ethylene glycol) tosylate and triol **3**, the allyl group in ether **4** was oxidized to the carboxylic group with *in situ* generated  $\text{RuO}_4$  to give branched M-PEG **5** with a yield of 23% over 3 steps on a multigram scale. The fluorinated methyl ester **9** was prepared by Mitsunobu ether formation between perfluoro-*tert*-butanol and triol **6** followed by transformation of the *tert*-butyl ester **7** into methyl ester **9** which was then transformed into amine **10** through aminolysis with ethylenediamine on a multigram scale. The fragment assembly started with the conjugation of fluorinated amine **10** with the orthogonally protected lysine to give amide **11** with a 64% yield. Selective removal of the Boc group in amide **11** followed by conjugation with branched OEG acid **5** provided amide **13** with a 73% yield over 2 steps. Finally, fluorinated amphiphile **1** was obtained on a multigram scale by removing the *Fmoc* group in amide **13** and conjugating with trimesic acid. Fluorinated amphiphile **1** was carefully characterized with HPLC (Fig. S1, ESI $^\dagger$ ),  $^1\text{H}/^{19}\text{F}/^{13}\text{C}$  NMR and MALDI-TOF mass spectrometry (ESI $^\dagger$ ).

As designed, amphiphile **1** showed high  $^{19}\text{F}$  MRI sensitivity and water solubility: (1) 81 symmetrical fluorines in amphiphile **1** collectively give a singlet  $^{19}\text{F}$  NMR peak (Fig. 2a). (2) Amphiphile **1** has high solubility in phosphate buffered saline (PBS) and no phase separation was observed at a high concentration of 15 mM.

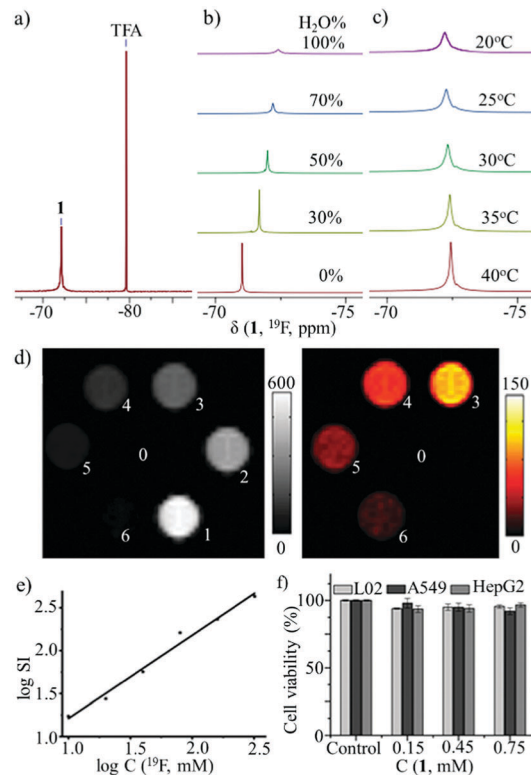
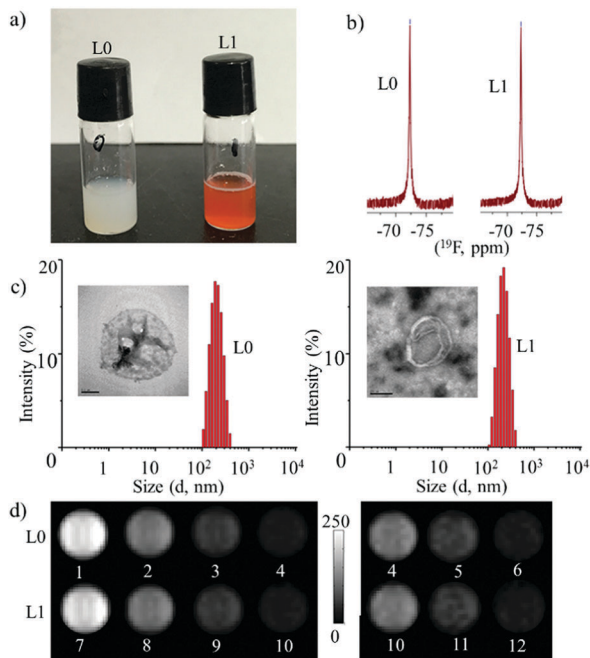


Fig. 2  $^{19}\text{F}$  NMR (a: 1.5 mM in  $\text{D}_2\text{O}$ , TFA as an internal standard), solvent-dependent  $^{19}\text{F}$  NMR (b: 1.5 mM in  $\text{MeOH}-\text{H}_2\text{O}$ ), temperature-dependent  $^{19}\text{F}$  NMR (c: 1.5 mM in  $\text{H}_2\text{O}$ ),  $^{19}\text{F}$  MRI *in vitro* images (d: two signal intensity scales are shown).  $^{19}\text{F}$  concentration of samples 0 to 6 are 0 mM, 320 mM, 160 mM, 80 mM, 40 mM, 20 mM, and 10 mM in  $\text{H}_2\text{O}$ ), the plot of signal intensity (SI) versus  $^{19}\text{F}$  concentration (e), and cytotoxicity assay (f) of amphiphile **1** on L02, A549, and HepG2 cells.

The aggregation of amphiphile **1** in water was confirmed by solvent- and temperature-dependent  $^{19}\text{F}$  NMR chemical shift changes (Fig. 2b and c).<sup>29</sup> (3) It has short longitudinal and transverse relaxation times ( $T_1 = 377$  ms and  $T_2 = 28$  ms, 3.8 mM in water, 25  $^\circ\text{C}$ ), which may enhance  $^{19}\text{F}$  MRI sensitivity by reducing the  $^{19}\text{F}$  MRI scan time.<sup>28–31</sup> (4)  $^{19}\text{F}$  MRI *in vitro* images showed high  $^{19}\text{F}$  MRI sensitivity of amphiphile **1** from which a clear image was obtained at a low concentration of 123.5  $\mu\text{M}$  with a scan time of 256 seconds (or 10 mM in  $^{19}\text{F}$  concentration, Fig. 2d). (5) The  $^{19}\text{F}$  MRI signal intensity of amphiphile **1** is proportional to its  $^{19}\text{F}$  concentration (Fig. 2e), which would be important for a downstream quantitative study.

Amphiphile **1** also exhibits high biocompatibility. Cytotoxicity assays using normal human hepatocyte cells (L02 cells), human lung adenocarcinoma cells (A549 cells), and hepatocellular carcinoma cells (HepG2 cells) show no obvious cytotoxicity of amphiphile **1** (Fig. 2f). In addition, no acute toxicity of amphiphile **1** on 2 groups of 3 Balb/c mice was observed at tail vein doses of 1.5  $\text{g kg}^{-1}$  and 3.0  $\text{g kg}^{-1}$  over 30 days, respectively.

Amphiphile **1**-based  $^{19}\text{F}$  MRI traceable liposomes were then formulated. Using the film dispersion method, liposome L0 and DOX-loaded (0.2  $\text{mg mL}^{-1}$ ) liposome L1 were prepared with both hydrogenated soy phosphatidylcholine (HSPC) and amphiphile **1**



**Fig. 3** Sample photos (a),  $^{19}\text{F}$  NMR (b,  $25^\circ\text{C}$ ), DLS and TEM images (c), and  $^{19}\text{F}$  MRI *in vitro* images (d,  $^{19}\text{F}$  concentration of samples from left to right are 160 mM, 80 mM, 40 mM, 20 mM, 10 mM, 5 mM, scan time: left 96 s; right 384 s) of fluorinated liposomes L0 and L1.

as surfactants and cholesterol as an additive (Fig. 3a). A high drug encapsulation efficiency of 91% was obtained for liposome L1. To improve the  $^{19}\text{F}$  MRI sensitivity, relatively large-sized liposomes with high amphiphile **1** loading were desired. Dynamic light-scattering (DLS) indicated that monodisperse liposomes L0 and L1 with narrow polydispersity indexes (PDI, L0: 0.124, L1: 0.117) and desired particle sizes (L0: 185 nm, L1: 189 nm) were obtained

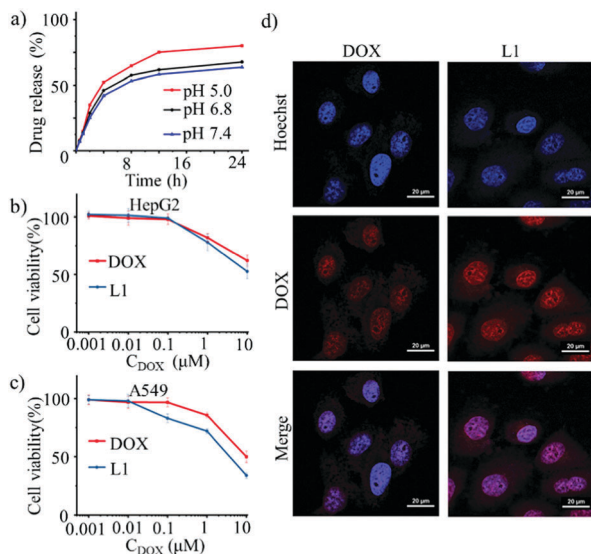


**Fig. 4** pH-Promoted DOX release of liposome L1 (a), antiproliferation efficiency of liposome L1 and DOX on HepG2 cells (b) and A549 cells (c), and confocal laser scanning microscopy of DOX and liposome L1 treated HepG2 cells (d).

(Fig. 3c and Table S1, ESI $^\dagger$ ). The transmission electron microscopy (TEM) image showed the liposomal spherical structure (Fig. 3c, insets). As expected, liposomes L0 and L1 showed a strong singlet  $^{19}\text{F}$  NMR peak (Fig. 3b). The  $^{19}\text{F}$  MRI *in vitro* images showed high  $^{19}\text{F}$  MRI sensitivity of these liposomes (Fig. 3d). With a scan time of 96 seconds, high resolution  $^{19}\text{F}$  images were obtained for liposomes L0 and L1 at a low  $^{19}\text{F}$  concentration of 20 mM (Fig. 3d, left). Upon extending the scan time to 384 seconds, the detectable  $^{19}\text{F}$  concentration can be lowered to 5 mM (Fig. 3d, right). In terms of the drug concentration in liposome L1,  $^{19}\text{F}$  MRI could trace DOX at 10  $\mu\text{M}$ , which is the first case of  $^{19}\text{F}$  MRI drug tracing around its *in vivo* therapeutic concentration (about 10.3  $\mu\text{M}$  for DOX).

The *in vitro* drug release and antiproliferation efficiency of liposome L1 were then evaluated with DOX as a control. On one hand, it was found that an acidic environment prompted the release of DOX from liposome L1 (Fig. 4a). On the other hand, the antiproliferative activity assay on the HepG2 cells and A549 cells showed that liposome L1 had comparable therapeutic efficiency to DOX (Fig. 4b and c). In addition, confocal laser scanning microscopy analysis indicated that DOX-loaded liposome L1 can cross the cell membrane and enter the cell much more efficiently than DOX (Fig. 4d). Therefore, liposome L1 is an effective drug delivery system for *in vitro* DOX cancer therapy.

Finally, a proof-of-concept study on *in vivo*  $^{19}\text{F}$  MRI-monitored DOX delivery was carried out. An intravenous injection of the amphiphile **1** solution at a  $^{19}\text{F}$  dose of 30 mmol  $\text{kg}^{-1}$  was employed to illustrate its biodistribution in nude mice (Fig. 5a-1, top).

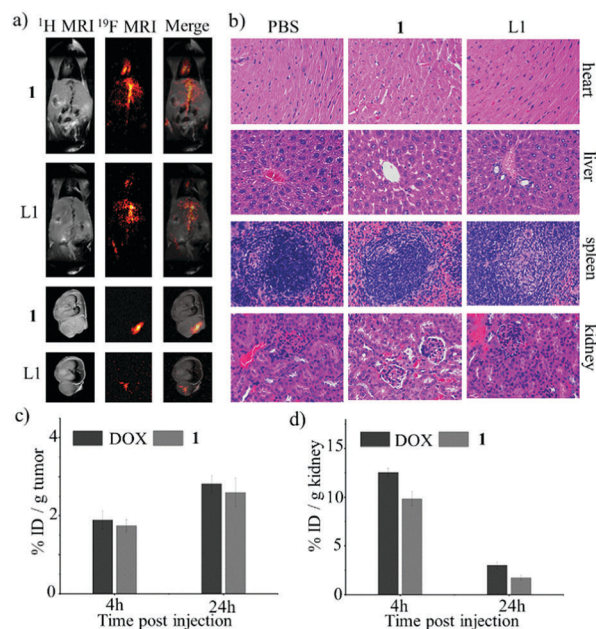


**Fig. 5** Mice  $^{19}\text{F}$  MRI of amphiphile **1** and liposome L1 (a, top, two mice images 1 h after an iv injection of **1** and L1, respectively; bottom, two tumor images 1 h after local injection of **1** and L1, respectively), pathological sections of organs after injection of PBS, amphiphile **1**, and liposome L1 (b), distribution of organs after injection of DOX and amphiphile **1** in tumor (c, %ID/g stands for the percentage of injected dose per gram tissue) and kidneys (d) 4 h and 24 h after iv injection of liposome L1 (5 mg  $\text{kg}^{-1}$  DOX).

$^{19}\text{F}$  MRI indicated that amphiphile **1** was soon distributed in the cardiovascular system and accumulated in the heart and liver. A therapeutic dose of DOX-loaded liposome L1 at 10 mmol kg $^{-1}$  of  $^{19}\text{F}$  (17.7  $\mu\text{mol kg}^{-1}$  of DOX) was used to monitor the biodistribution of the drug delivery system in nude mice (Fig. 5a-L1, middle).  $^{19}\text{F}$  MRI showed that liposome L1 was carried over by the cardiovascular system and gradually accumulated in the heart, liver, and kidneys which shows a slightly different biodistribution from the amphiphile **1** solution.  $^{19}\text{F}$  MRI of tumor-carrying nude mice with a local injection of amphiphile **1** and liposome L1 at  $^{19}\text{F}$  doses of 10 mmol kg $^{-1}$  and 3.3 mmol kg $^{-1}$ , respectively, showed the distribution of amphiphile **1** and liposome L1 in the tumor (Fig. 5a-1 and -L1, bottom). The internal organs were collected, and the pathological sections showed that both amphiphile **1** and liposome L1 induced negligible organ damage (Fig. 5b). The amount of DOX and amphiphile **1** in tumors and kidneys was quantitatively measured by HPLC and  $^{19}\text{F}$  NMR, respectively, which indicated the co-localization of DOX and amphiphile **1** *in vivo* (Fig. 5c and d). Therefore, fluorinated liposome L1 is a  $^{19}\text{F}$  MRI-traceable drug delivery system to efficiently monitor DOX *in vivo* at its therapeutic dose level.

In summary, we have developed a fluorinated dendritic amphiphile and applied it to formulate a  $^{19}\text{F}$  MRI-traceable liposomal drug delivery system.  $^{19}\text{F}$  MRI is not a very sensitive imaging modality which can hardly be employed to *in vivo* trace low concentration objects, such as drugs, genes, enzymes, antibodies, *etc.* To this end, the fluorine amphiphile-based liposomes provide a convenient and effective strategy. The fluorinated amphiphile is featured with 81 symmetrical fluorines and strong interaction with the liposomal membrane, which resulted in a uniform  $^{19}\text{F}$  NMR signal and high stability of the liposomal drug delivery system. The non-covalent encapsulation of drugs and  $^{19}\text{F}$  MRI agents not only provides the drug delivery system with high flexibility and convenience, but also avoids drug modification-induced therapeutic efficacy loss and case-by-case chemical modification. Incorporation of such multiple fluorinated amphiphiles with a uniform  $^{19}\text{F}$  NMR signal onto each liposomal nanoparticle provides the resulting liposomes with high  $^{19}\text{F}$  MRI sensitivity for *in vivo*  $^{19}\text{F}$  MRI tracing of DOX at its therapeutic dose level without radiolabelling, tissue depth limits, and background signals. Besides DOX, the fluorinated amphiphile-based liposomes may be employed as a general platform for tracing various drugs with  $^{19}\text{F}$  MRI at their therapeutic dose level. Tuning the target delivery and controlled release of DOX in tumor carrying mice and developing  $^{19}\text{F}$  MRI-guided DOX cancer therapy are currently in progress and will be published in due course.

We are thankful for financial support from the National Key Research and Development Program of China (2016YFC1304704), the National Natural Science Foundation of China (21372181, 21402144 and 21572168), the Major Project of Technology Innovation Program of Hubei Province (2016ACA126), and the State Key

Laboratory for Magnetic Resonance and Atomic and Molecular Physics (Wuhan Institute of Physics and Mathematics).

## Conflicts of interest

There are no conflicts to declare.

## Notes and references

- 1 Y. Liu, H. Miyoshi and M. Nakamura, *Int. J. Cancer*, 2007, **120**, 2527.
- 2 D. Ding, K. Li, Z. Zhu, K. Y. Pu, Y. Hu, X. Jiang and B. Liu, *Nanoscale*, 2011, **3**, 1997.
- 3 T. L. Doane and C. Burda, *Chem. Soc. Rev.*, 2012, **41**, 2885.
- 4 M. Chen, Y. He, X. Chen and J. Wang, *Bioconjugate Chem.*, 2013, **24**, 387.
- 5 Y. Yuan, R. T. Kwok, R. Zhang, B. Z. Tang and B. Liu, *Chem. Commun.*, 2014, **50**, 11465.
- 6 Y. Li, H. Chen, J. Xu, N. N. Yadav, K. W. Chan, L. Luo, M. T. McMahon, B. Vogelstein, P. C. van Zijl, S. Zhou and G. Liu, *Oncotarget*, 2016, **7**, 6369.
- 7 H. Liu, A. Jablonska, Y. Li, S. Cao, D. Liu, H. Chen, P. C. van Zijl, J. W. Bulte, M. Janowski, P. Walczak and G. Liu, *Theranostics*, 2016, **6**, 1588.
- 8 J. Ruiz-Cabello, B. P. Barnett, P. A. Bottomley and J. W. Bulte, *NMR Biomed.*, 2011, **24**, 114.
- 9 J. C. Knight, P. G. Edwards and S. J. Paisey, *RSC Adv.*, 2011, **1**, 1415.
- 10 Y. B. Yu, *Wiley Interdiscip. Rev.: Nanomed. Nanobiotechnol.*, 2013, **5**, 646.
- 11 I. Tirota, V. Dichiarante, C. Pigliacelli, G. Cavallo, G. Terraneo, F. B. Bombelli, P. Metrangolo and G. Resnati, *Chem. Rev.*, 2015, **115**, 1106.
- 12 E. T. Ahrens, R. Flores, H. Xu and P. A. Morel, *Nat. Biotechnol.*, 2005, **23**, 983.
- 13 J. M. Janjic, M. Srinivas, D. K. K. Kadayakkara and E. T. Ahrens, *J. Am. Chem. Soc.*, 2008, **130**, 2832.
- 14 S. Langereis, J. Keupp, J. L. J. van Velthoven, I. H. E. de Roos, D. Burdinski, J. A. Pikkemaat and H. Grull, *J. Am. Chem. Soc.*, 2009, **131**, 1380.
- 15 D. Vivian, K. Cheng, S. Khurana, S. Xu, E. H. Kriel, P. A. Dawson, J. P. Raufman and J. E. Polli, *Mol. Pharmaceutics*, 2014, **11**, 1575.
- 16 I. Tirota, A. Mastropietro, C. Cordiglieri, L. Gazzera, F. Baggi, G. Baselli, M. G. Bruzzone, I. Zucca, G. Cavallo, G. Terraneo, F. Baldelli Bombelli, P. Metrangolo and G. Resnati, *J. Am. Chem. Soc.*, 2014, **136**, 8524.
- 17 Y. Li, G. Xia, Q. Guo, L. Wu, S. Chen, Z. Yang, W. Wang, Z. Y. Zhang, X. Zhou and Z.-X. Jiang, *MedChemComm*, 2016, **7**, 1672.
- 18 Q. Shi, Y. Li, S. Bo, X. Li, P. Zhao, Q. Liu, Z. Yang, H. Cheng, H. Deng, M. Chen, S. Chen, X. Zhou, H. Ding and Z.-X. Jiang, *Chem. Commun.*, 2016, **52**, 5136.
- 19 J. Wang, M. Sánchez-Roselló, J. L. Aceña, C. del Pozo, A. E. Sorochinsky, S. Fustero, V. A. Soloshonok and H. Liu, *Chem. Rev.*, 2014, **114**, 2432.
- 20 Y. Zhou, J. Wang, Z. Gu, S. Wang, W. Zhu, J. L. Aceña, V. A. Soloshonok, K. Izawa and H. Liu, *Chem. Rev.*, 2016, **116**, 422.
- 21 J. M. Criscione, B. L. Le, E. Stern, M. Brenna, C. Rahner, X. Papademetris and T. M. Fahmy, *Biomaterials*, 2009, **30**, 3946.
- 22 S. Bo, C. Song, Y. Li, W. Yu, S. Chen, X. Zhou, Z. Yang, X. Zheng and Z.-X. Jiang, *J. Org. Chem.*, 2015, **80**, 6360.
- 23 W. Yu, Y. Yang, S. Bo, Y. Li, S. Chen, Z. Yang, X. Zheng, Z.-X. Jiang and X. Zhou, *J. Org. Chem.*, 2015, **80**, 4443.
- 24 H. Chen, M. Song, J. Tang, G. Hu, S. Xu, Z. Guo, N. Li, J. Cui, X. Zhang, X. Chen and L. Wang, *ACS Nano*, 2016, **10**, 1355.
- 25 G. Hu, J. Tang, X. Bai, S. Xu and L. Wang, *Nano Res.*, 2016, **9**, 1630.
- 26 G. Hu, N. Li, J. Tang, S. Xu and L. Wang, *ACS Appl. Mater. Interfaces*, 2016, **8**, 22830.
- 27 C. Guo, M. Xu, S. Xu and L. Wang, *Nanoscale*, 2017, **9**, 7163.
- 28 Z.-X. Jiang, X. Liu, E. K. Jeong and Y. B. Yu, *Angew. Chem., Int. Ed.*, 2009, **48**, 4755.
- 29 X. Liu, Y. Yuan, S. Bo, Y. Li, Z. Yang, X. Zhou, S. Chen and Z.-X. Jiang, *Eur. J. Org. Chem.*, 2017, 4461.
- 30 Q. Peng, Y. Yuan, H. Zhang, S. Bo, Y. Li, S. Chen, Z. Yang, X. Zhou and Z.-X. Jiang, *Org. Biomol. Chem.*, 2017, **15**, 6441.
- 31 A. A. Kislukhin, H. Xu, S. R. Adams, K. H. Narsinh, R. Y. Tsien and E. T. Ahrens, *Nat. Mater.*, 2016, **15**, 662.